JOURNAL OF MAGNETIC RESONANCE **133,** 46–52 (1998)
ARTICLE NO. MN981418

Two-Dimensional Nuclear-Zeeman-Resolved Electron Spin Echo Envelope Modulation (NZ-ESEEM) Spectroscopy

Michael Willer, Josef Granwehr, Jörg Forrer, and Arthur Schweiger[1]

Laboratorium für Physikalische Chemie, Eidgenössische Technische Hochschule, CH-8092 Zürich, Switzerland

Received September 23, 1997; revised January 13, 1998

A two-dimensional electron spin echo envelope modulation (ESEEM) experiment, called nuclear-Zeeman-resolved ESEEM (NZ-ESEEM), that correlates nuclear transition frequencies with nuclear Zeeman frequencies is introduced. NZ-ESEEM is basically a three-pulse ESEEM experiment complemented by a magnetic-field pulse applied during part of the free evolution period between the second and third microwave pulse. The inner working of the new approach is explained and the instrumentation is discussed. The capacity of the method is illustrated by two examples of applications. © 1998 Academic Press

Key Words: **pulse EPR; ESEEM; two-dimensional spectroscopy; magnetic field step.**

1. INTRODUCTION

Electron spin echo envelope modulation (ESEEM) techniques are widely used for measuring nuclear transition frequencies in paramagnetic species (*1, 2*). Although the spectral resolution of ESEEM is considerably higher than that of field-swept EPR, ESEEM spectra may be very complex and difficult to interpret. This is because the nuclear transition frequencies are often determined by hyperfine, nuclear Zeeman and nuclear quadrupole ($I \geq 1$) contributions that are similar in magnitude, so that many of the lines in the ESEEM spectrum overlap.

A number of two-dimensional correlation techniques have been introduced to disentangle complicated ESEEM spectra, either by separating the different energy contributions or by eliminating part of them. Hyperfine sublevel correlation (HYSCORE) experiments are used to correlate nuclear frequencies in different m_S-manifolds of the electron spin (*3–7*). Hyperfine spectroscopy allows the *direct* measurement of hyperfine splittings and their correlation with the corresponding nuclear transition frequencies (*8–10*), whereas with hyperfine-decoupling techniques, nuclear frequencies free of hyperfine interactions are correlated with the unaffected nuclear frequencies (*11, 12*).

In this article we introduce the two-dimensional (2D) experiment *n*uclear-*Z*eeman-resolved *ESEEM* (NZ-ESEEM), which allows the exclusive correlation of a nuclear frequency measured in an ESEEM experiment with the corresponding nuclear Zeeman frequency. In NZ-ESEEM the assignment of the nuclear frequencies to the particular types of nuclei or nuclear isotopes becomes definite. With NZ-ESEEM, combination lines can also be separated from the basic frequencies.

The approach, which is based on a scheme that uses microwave (mw) excitation in combination with a rapid stepping of the static magnetic field, has some analogy to electron-Zeeman-resolved EPR (*13*). The theoretical description of NZ-ESEEM is straightforward; the technical realization, however, is quite demanding. In this article we explain the basics of the technique, discuss the experimental setup, and illustrate the efficiency of the approach by two experimental examples.

2. THEORY

In first order, the nuclear Zeeman term

$$\mathcal{H}_{NZ} = \omega_I I_z = -g_n \beta_n B_0 I_z/\hbar \qquad [1]$$

is the only B_0-field sensitive interaction that contributes to a nuclear transition frequency. Since this term is a function of the nuclear g_n value, different types of nuclei show different behavior when the magnetic field is changed.

The NZ-ESEEM method is basically a three-pulse stimulated echo experiment, where the time between the second and third mw $\pi/2$ pulse is subdivided in two intervals, a variable time t_1 and a fixed time t_2 during which a magnetic-field step is applied (Fig. 1). The building block $\pi/2$–τ–$\pi/2$ creates nuclear coherence that freely evolves under the field B_0. After time t_1 a magnetic-field step ΔB_0 of length t_2 is applied to allow the nuclear coherence to accumulate additional phase. The nuclear coherence is then transferred to electron coherence by the third mw $\pi/2$ pulse and refocused to an electron spin echo at time τ after the pulse. In this 2D experiment the modulation of the echo amplitude is caused by the variable time t_1 and the variable magnetic field that is stepped from $-\Delta B_{0,max}$ to $+\Delta B_{0,max}$. In principle the order of the two time intervals t_1 and t_2 can be chosen arbitrarily, but for technical reasons it is of advantage to apply the B_0-field pulse after the free evolution under B_0. A 2D Fourier transformation then yields the 2D

[1] To whom correspondence should be addressed. Fax: +41/1/632 10 21. E-mail: schweiger@esr.phys.chem.ethz.ch.

1090-7807/98 $25.00

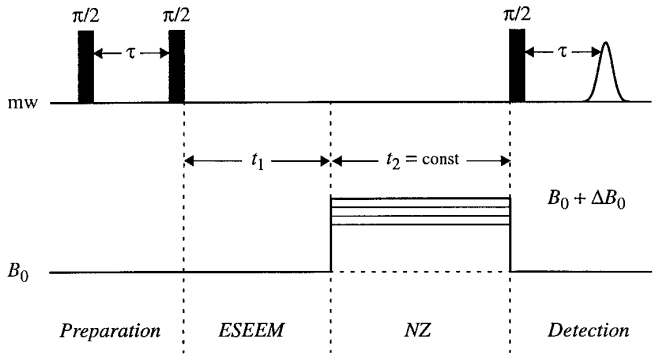

FIG. 1. Pulse sequence for the 2D NZ-ESEEM experiment with the variables t_1 (after Fourier transformation the ESEEM-dimension) and ΔB_0 (after Fourier transformation the g_n-dimension). Typical parameters: length of the magnetic-field pulse t_2 = 5–10 μs; length of the mw $\pi/2$ pulses 20 ns.

NZ-ESEEM spectrum with a nuclear frequency or ESEEM-dimension and a g_n value or NZ-dimension.

In first order the nuclear frequencies change linearly with B_0; thus, the frequency shifts caused by a variation of B_0 are directly proportional to the nuclear g_n factor and therefore characteristic for each nucleus. For a fixed time t_1, the Fourier transform of the modulation pattern recorded as a function of ΔB_0 results in the corresponding ''g_n-spectrum,''

$$s(\Delta B_0) \underset{\mathcal{F}^{-1}}{\overset{\mathcal{F}}{\rightleftharpoons}} S\left(g_n \frac{t_2 \beta_n}{h}\right). \qquad [2]$$

For a more detailed description of the NZ-ESEEM experiment, we consider an anisotropic $S = 1/2$, $I = 1/2$ electron-nuclear spin system. With the nucleus lying in the xz plane of the laboratory frame, the rotating frame spin Hamiltonian is given by

$$\mathcal{H}_0 = \Omega_S S_z + \omega_I I_z + A S_z I_z + B S_z I_x, \qquad [3]$$

where $\Omega_S = \omega_S - \omega_{mw}$ is the offset of the electron Zeeman frequency ω_S from the mw frequency ω_{mw}, and A and B are related to the elements A_{ij} of the hyperfine matrix by $A = A_{zz}$ and $B = (A_{zx}^2 + A_{zy}^2)^{1/2}$. For an axially symmetric hyperfine matrix with principal values $A_\parallel = 2T + a$ and $A_\perp = -T + a$,

$$\begin{aligned} A &= A_\parallel \cos^2\theta + A_\perp \sin^2\theta \\ B &= (A_\parallel - A_\perp)\sin\theta\cos\theta, \end{aligned} \qquad [4]$$

where $T = (\mu_0/4\pi) g g_n \beta_e \beta_n / r^3 \hbar$ is the point-dipole interaction with principal axes $(-T, -T, 2T)$, a is the Fermi contact term, r is the vector joining the electron spin and the nucleus, and θ is the angle between the principal axis $A_\parallel$ and the magnetic field vector $\boldsymbol{B}_0$.

Since NZ-ESEEM and three-pulse ESEEM are based on the same nuclear coherence transfer pathways, the analytical expression for the echo intensity in the NZ-ESEEM experiment is obtained by introducing a variable nuclear Zeeman interaction in the three-pulse ESEEM formula (*1*),

$$\begin{aligned} I_{Echo}(\tau, t_1, t_2, B_0) &= \frac{1}{2} - \frac{k}{8}\{C_\alpha(1 - \cos[\omega_\beta(\tau + t_1) + \omega'_\beta t_2]) \\ &\quad + C_\beta(1 - \cos[\omega_\alpha(\tau + t_1) + \omega'_\alpha t_2])\}, \end{aligned} \qquad [5]$$

with the coefficients

$$C_{\alpha,\beta} = 1 - \cos(\omega_{\alpha,\beta}\tau) \qquad [6]$$

and the nuclear transition frequencies

$$\begin{pmatrix} \omega_\alpha \\ \omega_\beta \end{pmatrix} = \left[\left(-\frac{g_n \beta_n B_0}{\hbar} \pm \frac{A}{2}\right)^2 + \left(\frac{B}{2}\right)^2\right]^{1/2} \qquad [7]$$

$$\begin{pmatrix} \omega'_\alpha \\ \omega'_\beta \end{pmatrix} = \left[\left(-\frac{g_n \beta_n (B_0 + \Delta B_0)}{\hbar} \pm \frac{A}{2}\right)^2 + \left(\frac{B}{2}\right)^2\right]^{1/2}. \qquad [8]$$

During the fixed time t_2, the nuclear frequencies evolve with ω'_α and ω'_β. According to Eq. [2], the Fourier transform in the NZ-dimension is given by

$$S_{\alpha,\beta}\left(g_n \frac{t_2 \beta_n}{h}\right) = \frac{k}{8} C_{\beta,\alpha} \int_{-\infty}^{\infty} \cos(\omega'_{\alpha,\beta} t_2 + \varphi_{\alpha,\beta}) e^{-i2\pi g_n (t_2 \beta_n / h)\Delta B_0} d\Delta B_0, \qquad [9]$$

with phases $\varphi_{\alpha,\beta} = \omega_{\alpha,\beta}(\tau + t_1)$.

Figure 2 shows the dependence of the weighted nuclear frequencies ω_α/a and ω_β/a in the two m_S-manifolds (see Eq. [5]) on the weighted nuclear Zeeman interaction $|\omega_I|/a$, with $T = (3/5)a > 0$, $\theta = 45°$, and $\omega_I < 0$ (as for protons). The solid lines include the pseudo-secular contributions ($B > 0$); the dashed lines are calculated with $B = 0$. Three of the $|\omega_I|/a$ values are marked by (a), (b), and (c). The corresponding vertical gray-shaded bars indicate the range of $|\omega_I|/a$ covered by $\Delta B_0 = \pm 20$ mT, corresponding to the maximum field step that has been realized experimentally in this work.

Neglecting pseudo-secular contributions, ω'_α and ω'_β are linear in ΔB_0. This approximation is, however, only valid in the limiting case of weak or strong hyperfine coupling. In the next section, we will demonstrate that the pseudo-secular contributions may considerably influence the values in the g_n-dimension of the NZ-ESEEM spectra.

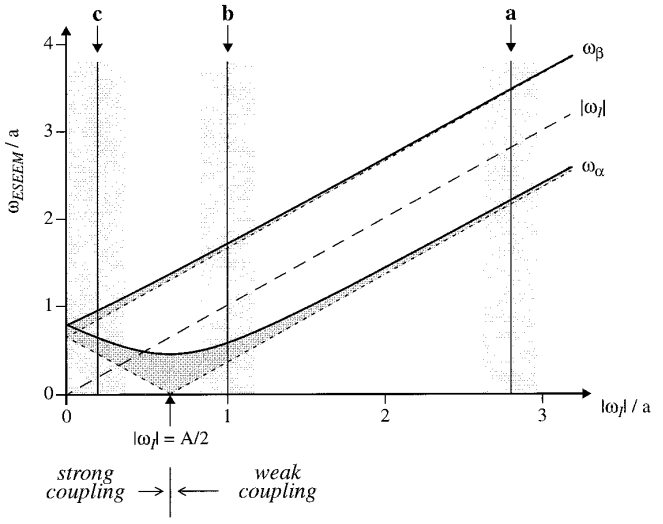

FIG. 2. Weighted nuclear transition frequencies ω_α/a and ω_β/a for an $S = 1/2$, $I = 1/2$ model system as a function of the weighted nuclear Zeeman frequency $|\omega_I|/a$. An axially symmetric hyperfine interaction is assumed, with the isotropic hyperfine coupling constant a and the dipolar coupling constant $T = (3/5)a$. The frequencies are calculated for $\theta = 45°$ (maximum modulation depth). Strong and weak coupling regions are indicated. The full lines include pseudo-secular contributions ($B > 0$); the dashed lines are calculated with $B = 0$. In the α-manifold the pseudo-secular term prevents the transition frequency ω_α from approaching zero (sublevel noncrossing). Positions (a), (b), and (c) refer to the simulations in Fig. 3. For each of the three positions the variation in $|\omega_I|/a$ for the maximum $\pm\Delta B_0$ field step (20 mT) is indicated by vertical gray-shaded bars.

3. NUMERICAL COMPUTATIONS

To get some insight into how NZ-ESEEM spectra manifest for typical sets of coupling parameters, numerical simulations have been carried out with the program GAMMA (*14*). All three contour plots shown in Fig. 3 represent absolute-value spectra, obtained after baseline correction, apodization with a Hamming window, and 2D Fourier transformation. The NZ-dimension has been recalculated according to

$$g'_{n,max} = \frac{1}{2\Delta(\Delta B_0)} f(t_2), \qquad [10]$$

where $\Delta(\Delta B_0)$ is the incrementation of the ΔB_0 field and $f(t_2) = h/(\beta_n t_2)$. The primed g_n factor indicates that due to pseudo-secular contributions, $|g'_n| \leq |g_n|$ (see later discussion). Since the NZ-ESEEM time domain data are real, the two hemiplanes of the 2D plot contain the same spectral information; it is therefore sufficient to present only the positive values of the ESEEM-dimension. This is in analogy to HYSCORE, where the first two quadrants also contain the full spectral information.

Figure 3a represents a weak coupling situation, $A \ll 2|\omega_I|$, corresponding to a nuclear Zeeman interaction marked by (a) in Fig. 2. The frequencies $\omega_{\alpha 1}$ and $\omega_{\beta 1}$ are almost linearly dependent on B_0 (small pseudo-secular contributions). In the 2D plot the two peaks are found in the g_n-dimension at the proton value $g_n = 5.5857$, separated in the ESEEM-dimension by the hyperfine splitting $a_1 \approx a + T/2$.

In the intermediate coupling region, $A \approx 2|\omega_I|$, the g'_n value of the $\omega_{\alpha 2}$ transition is considerably smaller than g_n, and the peak is broadened along the NZ-dimension (Fig. 3b). This broadening is caused by the large nonlinearity between $\omega_{\alpha 2}$ and ω_I (see region (b) in Fig. 2). An analytical expression for the lineshape along the g'_n-dimension is given in (*15*).

In the strong coupling case, $A > 2|\omega_I|$, the peaks at frequencies $\omega_{\alpha 3}$ and $\omega_{\beta 3}$ are found in different quadrants (Fig. 3c) with g'_n values considerably lower than the proton g_n value (see position (c) in Fig. 2).

In first order the resolution in the NZ-dimension is determined by the maximum amplitude $\Delta B_{0,max}$ and the length t_2. For the minimum g_n value difference $\Delta g_{n,min}$ that can be resolved for a given $\Delta B_{0,max}$ and t_2, we find

$$\Delta g_{n,min} = \|g_{n1}| - |g_{n2}\| = \frac{f(t_2)}{\Delta B_{0,max}} = \frac{h}{\beta_n t_2 \Delta B_{0,max}}. \qquad [11]$$

In Table 1, minimum pulse lengths $t_{2,min}$ for resolving peaks of two nuclei with different g_n values and $\Delta B_{0,max} = 20$ mT are collected.

4. EXPERIMENTAL

4.1. Instrumentation

The main characteristics of a setup for the generation of short magnetic-field pulses are the time constant, the maximum achievable field step, and the homogeneity of the magnetic field produced by the pulse. In this section we describe a device for the generation of magnetic-field pulses of high homogeneity and variable length and amplitude.

Probehead. The mw part of the probehead consists of a loop-coupled bridged loop-gap resonator (BLGR) and a wire-wound shield. The BLGR is virtually transparent to high-frequency fields and was originally developed for experiments with rapid magnetic-field steps; its reliability and characteristics have been described earlier (*16, 17*). To prevent the formation of eddy currents, the resonator is surrounded by an open-ended solenoidal mw shield (copper wire, diameter 0.1 mm, pitch 0.15 mm, 50 windings). The holder for the BLGR and the mw shield are made of Rexolite. The metallic radiation shield of the dewar is removed in the field-jump coil area. The shield of the semirigid mw coaxial cable (EZ 86 Cu) that feeds to the coupling loop is cut in its lower part (20 mm) along the cable axis (groove width 0.5 mm). For critical coupling or overcoupling the coupling loop (silver-plated brass wire, diameter 0.8 mm, inner loop diameter 4.4 mm) can be moved along the sample axis.

Field jump coil. The pulsed magnetic field with a high homogeneity across the sample volume is created by high-

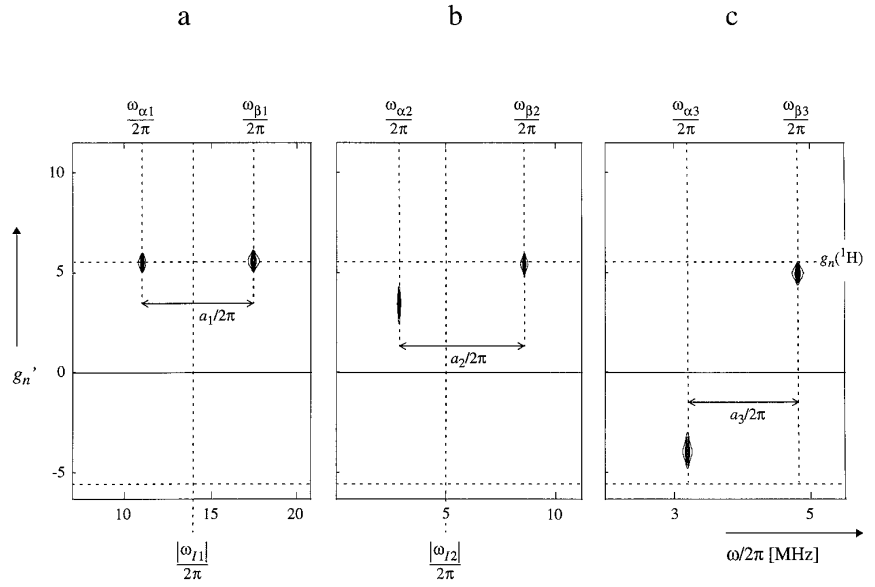

FIG. 3. Numerical simulations of the NZ-ESEEM experiment for an $S = 1/2$, $I = 1/2$ model system. Simulations (a), (b), and (c) refer to positions (a), (b), and (c) in Fig. 2. The following parameters representing typical experimental situations are used: $a/2\pi = 5$ MHz, $T/2\pi = 5$ MHz, $\theta = 45°$, g_n (^{1}H) = 5.5857, $t_2 = 10$ μs. (a) Weak coupling: $\omega_I/2\pi = -14$ MHz, $\tau = 300$ ns. (b) Intermediate coupling: $\omega_I/2\pi = -5$ MHz, $\tau = 200$ ns. (c) Strong coupling: $\omega_I/2\pi = -1$ MHz, $\tau = 250$ ns.

current pulses fed through a Helmholtz coil, consisting of two flat coils with a mean diameter of $d = 26$ mm positioned outside the mw shield, $z = 11$ mm apart form each other. Each coil consists of 17 turns of insulated copper wire (diameter 0.1 mm), wound uniformly in a single layer of circular grooves cut into a Rexolite holder. The coils fit into the helium gas flow dewar and are electrically connected in series ($L = 23$ μH at 25 MHz). The time-dependent magnetic field in the center of the Helmholtz coil is given by

$$\Delta B(t) = \Delta B_0 e^{-t/\tau_C}[1 - e^{-t/\tau_L}], \qquad [12]$$

with

$$\Delta B_0 = \mu_0 \left(\frac{4}{5}\right)^{3/2} \frac{NI}{z}. \qquad [13]$$

TABLE 1

Minimum Time $t_{2,min}$ Required to Separate Peaks of Different Nuclei from Each Other by Applying a Maximum B_0-Field Step of 20 mT

Nucleus 1	Nucleus 2	g_{n1}	g_{n2}	$t_{2,min}$ (μs)
^{1}H	^{2}H	5.5857	0.8574	1.38
^{1}H	^{14}N	5.5857	0.4038	1.27
^{1}H	^{19}F	5.5857	5.2577	20.0
^{1}H	^{31}P	5.5857	2.2632	1.97
^{1}H	^{35}Cl	5.5857	0.5479	1.30
^{14}N	^{31}P	0.4038	2.2632	3.53

N is the total number of turns, and τ_L and τ_C are the time constant of the coil and the discharge time constant of the capacitor, respectively. Since $\tau_L \ll \tau_C$, the shape of the pulses is mainly determined by τ_L (see later discussion).

Switching electronics. The current pulse circuit consists of two identical high-voltage modulation units shown in Fig. 4 (*18*). Each of them is designed to produce current pulses up to $I_p = 14$ A at a voltage of $U_C = 700$ V. The two modulation units are parallel connected to the coaxial cable (RG 233,

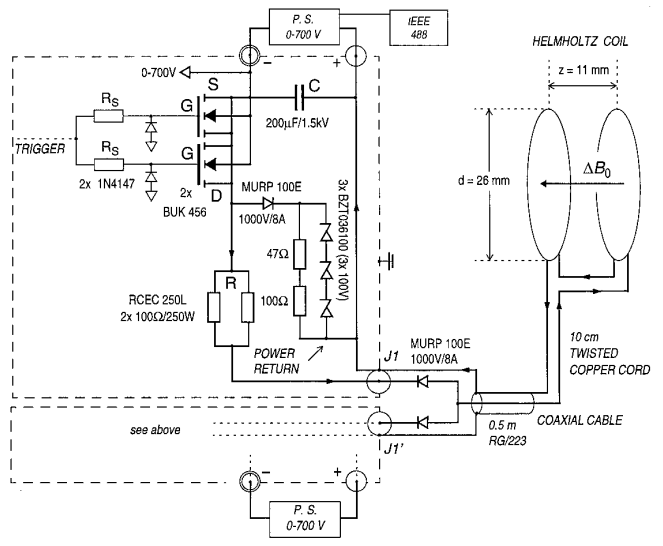

FIG. 4. Schematic diagram of the switching electronics for the generation of current pulses.

length 0.5 m) with two fast-recovery high-voltage diodes. The capacitor C (200 μF, 1.5 kV) is continuously charged by an IEEE-488 bus-controlled power supply (F.u.G. HCK 800-3500, U_c = 0–700 V/400 mA) and discharged by a high-power transistor switch (Power MOSFET, BUK 456-1000B, Philips) to generate the pulse current $I_p = U_C/(R + R_L)$ that passes through the Helmholtz coil. R_L (4.7 Ω at 298 K) is the resistance of the coil and R (50 Ω) is the resistance of two parallel high-power resistors (RCEC 250 L, 100 Ω, 250 W). The discharge time constant of the capacitor is $\tau_C = C(R+R_L) = 10.8$ ms, so that $U_C(t) \approx U_{C,0}$ for a typical length of the ΔB_0-field step of t_2 = 10 μs. The rise time is given by $\tau_{L,on} = L/(R+R_L) = 414$ ns. The power return path contains a fast recovery diode (MURP 100 E, 8 A, 1000 V) and two additional resistors (100 + 47 Ω) that shorten the discharge time of the coil and reduce the fall time to $\tau_{L,off}$ = 285 ns. The high-voltage spikes induced by the Helmholtz coil are limited to 300 V by three Zener diodes (BZT036100, 100 V) connected parallel to the resistors (Fig. 4). The maximum drain source voltage is therefore limited to 1000 V. From output J1 the two combined modulation units deliver the high-current pulse (2 I_p = 0–28 A) to the probehead. The feed through the probehead to the coils is made of a flexible copper cord (length 100 mm, diameter 0.2 mm) with additional Teflon insulation.

During the application of the field step the power is mainly dissipated in the two high-power resistors (MCB RCEC250, 100 Ω, 250 W), which are mounted on cooling plates. The fastest repetition rate is therefore given by

$$rr_{max} = \frac{P_R}{U_C I_p t_2}, \qquad [14]$$

with the maximum allowed power dissipation P_R and the pulse power $U_C I_p$. In the experiment ($t_2 \approx 10$ μs), however, rr is limited to about 500 Hz because of temperature effects.

4.2. Experimental Limitations

Apart from the pseudo-secular contribution of the hyperfine interaction, there are also experimental limitations leading to nonlinear behavior of the NZ-ESEEM experiment. The application of magnetic-field steps is limited by the inhomogeneity of the ΔB_0 field, which consists of a time-independent part determined by the geometrical arrangement of the Helmholtz coil, and a time-dependent part caused by the eddy currents generated in the metallic elements close to the sample.

Linearity and homogeneity of ΔB_0. Imperfections of the pulsed magnetic field may lead to spectral distortions. The most pronounced ones are caused by the magnetic-field inhomogeneity. Experimentally, the homogeneity has been determined via the FID of a single crystal of lithium phthalocyanin (room temperature, standard sample tube, 3.5 mm i.d.) observed after a mw $\pi/2$ pulse and $0 \le \Delta B_0 \le 22$ mT with $B_0 + \Delta B_0$ = const. To allow for the eddy currents to decay, a time delay of 7 μs between the B_0-field step and the mw pulse is introduced. The inhomogeneity of the ΔB_0 field leads to a broadening of the line in the FT-EPR spectrum from 0.25 to 2.00 MHz. NZ-ESEEM experiments are, however, not very sensitive to ΔB_0 inhomogeneities, since the intrinsic linewidth in the NZ-dimension is comparatively large.

Another effect that is caused by the ΔB_0 inhomogeneity shows up when the voltage $U_{C,0}$ is incremented. At higher voltage a deviation from the linear behavior is observed, since the ΔB_0 steps become slightly smaller. In principle, this can be compensated by a nonlinear incrementation scheme for $U_{C,0}$; however, since the deviation between the different steps is smaller than 5%, a linear regression with a conversion factor defined by

$$m(T) = \Delta B_0 / U_{C,0} \qquad [15]$$

has been used. Since at cryogenic temperatures the resistance R_L of the coil is drastically reduced, the conversion factor increases with decreasing temperature. The results of the calibration are $m = (1.8433 \pm 0.0184) \cdot 10^{-2}$ mT/V at T = 21.5 K, and $m = (1.6847 \pm 0.0226) \cdot 10^{-2}$ mT/V at T = 298 K, for each of the two units.

Transient ΔB_0*-field imperfections.* If the last mw $\pi/2$ pulse is applied immediately after the ΔB_0-field step is switched off, the falling edge of ΔB_0 causes the electron coherence to accumulate phase during the evolution period of time τ that is proportional to the average magnetic field. One can easily get rid of this phase change by using quadrature detection and calculating absolute-value spectra. One should, however, not extend this phase accumulation to angles larger than 2π. Assuming a maximum field step of $\Delta B_{0,max}$ = 20 mT and an evolution period of τ = 300 ns, this corresponds to a minimum waiting time of about 5.5 $\tau_{L,off}$, before the third mw pulse is applied. The imbalance of the two detection channels has been corrected using the CYCLOPS (*cycl*ically *o*rdered *p*hase *s*equence) procedure (*19, 20*).

5. EXPERIMENTAL RESULTS

The experiments have been carried out with a homebuilt high-power X-band cw/pulse EPR spectrometer (*21*) at a temperature of 16 K and an mw frequency of 9.456 GHz. The echo signals have been measured with a boxcar averager (PAR model 162 with a gated integrator model 165).

The NZ-ESEEM spectra were recorded using quadrature detection with the full CYCLOPS for the three mw $\pi/2$ pulses of duration t_p = 20 ns; other parameters: τ = 210 ns, length of the ΔB_0-field step t_2 = 10 μs, starting value $t_1(0)$ = 1.3 μs, time increment Δt_1 = 20 ns. The voltage has been increased in steps of ΔU_C = 25 V, corresponding to a field-step increment of $\Delta(\Delta B_0) = 0.4830$ mT (conversion factor $m = 1.9321 \cdot 10^{-2}$ mT/V). The data matrix consisted of 81 points in the NZ-

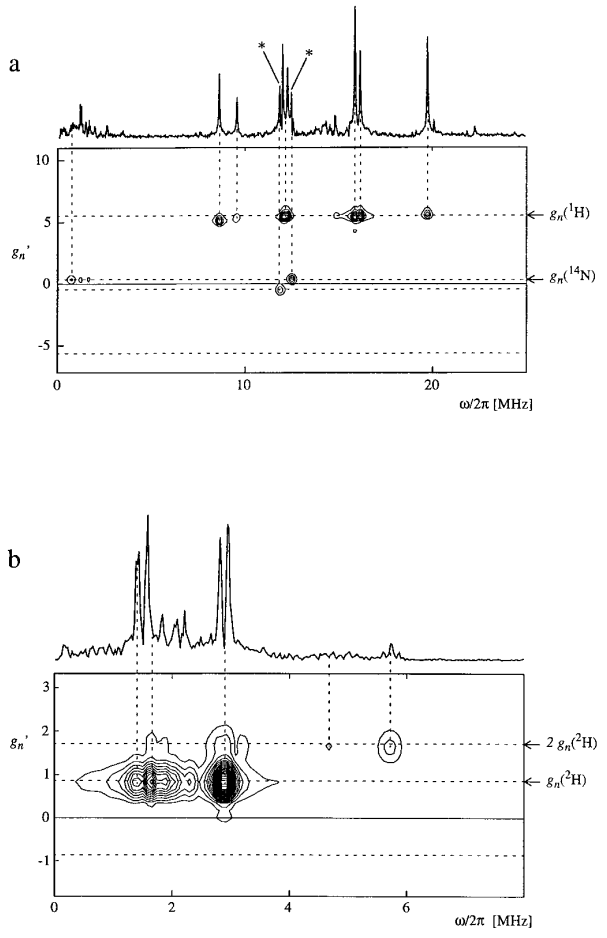

FIG. 5. (a) Three-pulse ESEEM spectrum and corresponding NZ-ESEEM contour plot of bis(glycinato)Cu(II) in an α-glycine single crystal at arbitrary orientation. The asterisks label two lines in the quartet that can be assigned with the help of NZ-ESEEM to ^{14}N nuclear transitions. Experimental parameters: see text. (b) Three-pulse ESEEM spectrum and corresponding NZ-ESEEM contour plot of bis(glycinato)Cu(II) in a deuterated triglycine sulfate single crystal at arbitrary orientation. Experimental parameters: see text.

dimension (symmetric to $\Delta B_0 = 0$) and 256 points in the ESEEM dimension. The data were baseline corrected, apodized with Hamming windows (symmetric in the NZ-dimension), zero-filled, and 2D Fourier transformed; absolute-value spectra are shown. For comparison, the corresponding three-pulse ESEEM trace was recorded with much higher resolution (starting value $T_0 = 500$ ns, time increment $\Delta T = 10$ ns, 3000 data points).

5.1. Separation of Overlapping ESEEM Lines

The improvement in resolution is demonstrated on an α-glycine single crystal doped with bis(glycinato)Cu(II). In this copper complex the nuclear transitions of the directly coordinated ^{14}N ligands lie in the proton frequency range and can easily be observed with ESEEM (*22*). Figure 5a shows the three-pulse ESEEM spectrum together with the contour plot of the NZ-ESEEM experiment. Despite of the lower resolution of the 2D plot in the ESEEM-dimension, the outer two lines of the quartet at about 12 MHz can unequivocally be assigned to ^{14}N nuclear transitions. The nitrogen peak at higher frequency appears in the first quadrant of the g_n'-dimension; the nitrogen peak at lower frequency appears in the second quadrant (strong coupling case). All the proton peaks, however, appear in the first quadrant (weak coupling case). The two proton ESEEM transitions close to 9 MHz slightly deviate from the $g_n(^1H)$ value in the NZ-dimension; this is the result of the increasing influence of the pseudo-secular term at lower frequencies. ESEEM transitions between 1 and 3 MHz stem from weakly coupled nitrogens of neighboring glycine molecules.

5.2. Identification of Combination Lines

For nuclei with $I > 1/2$, such as ^{14}N or ^{2}H, transitions with $\Delta m_I = \pm 2$ gain in intensity in strong mixing situations. Since these transitions evolve with twice the nuclear Zeeman frequency ω_I, they produce peaks at $2g_n$ in the NZ-dimension. The same is true for combination harmonics of different $I = 1/2$ nuclei within the same m_S-manifold that can occur in three-pulse ESEEM experiments.

The contour plot of an NZ-ESEEM spectrum of bis(glycinato)Cu(II) in a single crystal of deuterated triglycine sulfate is shown in Fig. 5b. The cross-peak at 5.7 MHz in the ESEEM-dimension and close to $2g_n$ (^{2}H) = 1.71 in the NZ-dimension is assigned to a combination harmonic of the two strong peaks close to 3 MHz. The very weak cross-peak at 4.7 MHz in the ESEEM-dimension is probably a combination harmonic of two basic frequencies of weakly coupled ^{2}H nuclei with basic frequencies in the range 1.8–3.8 MHz. Note that in the standard ESEEM spectrum the signal intensity of this peak is comparable to the level of the noise. However, since NZ-ESEEM introduces a new dimension with only a few discrete values, the method allows one in some favored cases to distinguish between weak signals and noise. Such an identification of ESEEM lines is especially useful in strong mixing situations, where peaks are expected even at higher multiples of g_n. This is particularly true for protons in the S-band frequency range (*23*). On the other hand, second-order effects can also complicate an NZ-ESEEM experiment, making a correct g_n assignment difficult (see Section 3).

6. CONCLUSION

The NZ-ESEEM experiment introduced in this work allows one to spread an ESEEM spectrum into a second dimension, according to the g_n values of the individual ESEEM transitions. Although the nuclear Zeeman interaction is not as sensitive to variations of the B_0 field as the electron Zeeman term in EZ-resolved EPR, the new experimental scheme can very successfully be applied to assign the ESEEM transitions of a large number of nuclei (see Table 1).

For disordered systems such as powders and frozen solutions, the three-pulse NZ-ESEEM approach is usually not applicable in this form, since the nuclear coherence decays within several microseconds. In such a situation we propose a four-pulse NZ-ESEEM experiment, with an mw π pulse applied prior to the ΔB_0-field step to refocus the nuclear coherence to a nuclear coherence transfer echo (*24*).

A simple way of correlating the nuclear Zeeman interaction of a nucleus with the nuclear transition frequency has been realized earlier in the continuous-wave experiment, called nuclear-Zeeman-correlated ENDOR (*25*), a scheme that requires well-separated and symmetric transitions in the corresponding field-swept EPR spectrum. In time-domain pulse ENDOR experiments, nuclear coherence can be generated by pulses of fixed or chirped radio frequencies (*26–28*). Combining the nuclear Zeeman approach with such an ENDOR scheme results in a 2D *N*uclear-*Z*eeman-resolved *ENDOR* (NZ-ENDOR) experiment, which we consider as a promising alternative to NZ-ESEEM.

ACKNOWLEDGMENT

This research has been supported by the Swiss National Science Foundation.

REFERENCES

1. W. B. Mims, *Phys. Rev.* **B5,** 2409 (1972).
2. S. A. Dikanov and Yu. D. Tsvetkov, ''Electron Spin Echo Envelope Modulation (ESEEM) Spectroscopy.'' CRC, Boca Raton (1992).
3. P. Höfer, A. Grupp, H. Nebenführ, and M. Mehring, *Chem. Phys. Lett.* **132,** 279 (1986).
4. J. J. Shane, P. Höfer, E. J. Reijerse, and E. de Boer, *J. Magn. Reson.* **99,** 596 (1992).
5. P. Höfer, *J. Magn. Reson. A* **111,** 77 (1995).
6. C. Gemperle, G. Aebli, A. Schweiger, and R. R. Ernst, *J. Magn. Reson.* **88,** 241 (1990).
7. M. Hubrich, G. Jeschke, and A. Schweiger, *J. Chem. Phys.* **104,** 2172 (1996).
8. Th. Wacker and A. Schweiger, *Chem. Phys. Lett.* **191,** 136 (1992).
9. G. Jeschke and A. Schweiger, *Chem. Phys. Lett.* **246,** 431 (1995).
10. G. Jeschke and A. Schweiger, *J. Magn. Reson. A* **119,** 45 (1996).
11. G. Jeschke and A. Schweiger, *Chem. Phys. Lett.* **231,** 574 (1994).
12. G. Jeschke and A. Schweiger, *J. Chem. Phys.* **106,** 9979 (1997).
13. G. A. Sierra, A. Schweiger, and R. R. Ernst, *Chem. Phys. Lett.* **184,** 363 (1991).
14. S. A. Smith, T. O. Levante, B. H. Meier, and R. R. Ernst, *J. Magn. Reson. A* **106,** 75 (1994).
15. J. Granwehr, Diploma Thesis, Laboratory for Physical Chemistry, ETH Zürich (1996).
16. S. Pfenninger, Ph.D. Thesis, ETH Zürich, No. 9602 (1991).
17. S. Pfenninger, J. Forrer, A. Schweiger, and Th. Weiland, *Rev. Sci. Instr.* **59,** 752 (1988).
18. J. Forrer, S. Pfenninger, G. Sierra, G. Jeschke, A. Schweiger, B. Wagner, and Th. Weiland, *Appl. Magn. Reson.* **10,** 263 (1996).
19. D. I. Hoult and R. E. Richards, *Proc. R. Soc. Lond.* **344,** 311 (1975).
20. D. D. Trafficante, *Concepts in Magnetic Resonance* **2,** 181 (1990).
21. Th. Wacker, Ph.D. Thesis, ETH Zürich, No. 9913 (1992).
22. M. Fujimoto, C. A. McDowell, and T. Takui, *J. Chem. Phys.* **70,** 3694 (1970).
23. M. Willer, Ph.D. Thesis, ETH Zürich, No. 12201 (1997).
24. A. Ponti and A. Schweiger, *J. Chem. Phys.* **102,** 5207 (1995).
25. M. Rudin, J. Forrer, and A. Schweiger, *J. Magn. Reson.* **54,** 447 (1983).
26. P. Höfer, A. Grupp, and M. Mehring, *Phys. Rev.* **A33,** 3579 (1986).
27. H. Cho, *J. Chem. Phys.* **94,** 2482 (1991).
28. G. Jeschke and A. Schweiger, *J. Chem. Phys.* **103,** 8329 (1995).